



In-situ hydrothermal fabrication of $\text{Sr}_2\text{FeTaO}_6/\text{NaTaO}_3$ heterojunction photocatalyst aimed at the effective promotion of electron-hole separation and visible-light absorption

Entian Cui^{a,1}, Guihua Hou^{a,1}, Xiahui Chen^b, Feng Zhang^a, Yuxin Deng^a, Guiyun Yu^a, Baibai Li^a, Yuqi Wu^{c,*}

^a Key Laboratory for Advanced Technology in Environmental Protection of Jiangsu Province, Yancheng Institute of Technology, Yancheng, 224051, China

^b School of Electrical, Computer and Energy Engineering Arizona State University Tempe, AZ, 85287, USA

^c State Key Laboratory for Oxo Synthesis and Selective Oxidation, Lanzhou Institute of Chemical Physics, Chinese Academy of Sciences, Lanzhou, 730000, China

ARTICLE INFO

Keywords:

Photocatalyst
Tantalate materials
Heterostructure
Transitional zone space
Electron-hole
Separation

ABSTRACT

The $\text{Sr}_2\text{FeTaO}_6/\text{NaTaO}_3$ heterojunctions with the controllable molar ratio and space of heterojunction transitional zone were fabricated using in situ hydrothermal method by adjusting hydrothermal temperature and time. Comparing with the pure NaTaO_3 nanosheets and $\text{Sr}_2\text{FeTaO}_6$ nanoparticles, the $\text{Sr}_2\text{FeTaO}_6/\text{NaTaO}_3$ heterojunctions exhibit higher photocatalytic performances, due to introducing narrow-bandgap $\text{Sr}_2\text{FeTaO}_6$ component, which could obviously enhance its absorbability in visible light region and separation efficiency of photo-generated electron-hole pairs. Under visible light irradiation, the optimal $\text{Sr}_2\text{FeTaO}_6/\text{NaTaO}_3$ heterojunction, with the molar ratio of 0.53 and space of heterojunction transitional zone of 0.35 nm, shows the best photocatalytic activity with the NO removal ratio of 72% in 40 min, hydrogen evolution rate of $1334 \mu\text{mol h}^{-1} \text{g}^{-1}$ in 5 h, and apparent quantum efficiency (AQE) for hydrogen evolution of 38.8% at 420 nm. More interestingly, the space of heterojunction transitional zone, related to the interface bonding degree of heterojunction material, may not be the only factor which influences transferring and separating efficiency of photo-generated charge carriers, but it is certainly an important one, which provides a new cognitive perspective for constructing and understanding efficient heterostructure photocatalyst.

1. Introduction

The solar-induced photocatalytic technology has been considered to be the most promising way to cope with the energy shortage and environmental pollution resulted from the large consumption of fossil fuels. Among the various photocatalysts, the tantalum-based semiconductor material $\text{M}_x\text{Ta}_y\text{O}_z$, as one kind of the promising photocatalyst, is widely used in the fields of pollutant degradation, water splitting, and CO_2 immobilization [1–6]. Within them, NaTaO_3 is the most important one, not only for its excellent stability, but also its strong redox ability, originating from its more negative conduction band (CB) and more positive valence band (VB) than most of the well-known photocatalytic materials [7–9]. However, the large bandgap and rapid recombination of photo-generated charge carriers have immensely restricted its photocatalytic efficiency and application potential. To solve them, various strategies such as doping [10,11], noble-

metal loading [12], and different crystal facets exposing [13], have been used and attempted. Constructing NaTaO_3 -based heterojunctions with narrow-bandgap semiconductor, such as $\text{CdS}/\text{Ta}_2\text{O}_5$ [14], $\text{In}_2\text{O}_3/\text{Ta}_2\text{O}_5$ [15], $\text{Bi}_2\text{O}_3/\text{Bi-NaTaO}_3$ [16], $\text{NiO}/\text{NaTaO}_3$ [17], have been proved to be an appropriate and effective solution, which based on two critical insights: One is, the potential gradient between tantalum-based and narrow-bandgap semiconductors can offer the transfer driving force and thus dominate the efficient transfer and separation of photo-generated charge carriers; And the other is, constructing the heterojunctions with narrow-bandgap semiconductor can increase the light responsivity at the visible-light (long wavelength) range.

But even so, the photocatalytic efficiencies of tantalum-based heterojunction materials are still to be further improved, because the unexpected defects at the interfaces can act as hole-electron recombination centers [18]. Therefore, developing well-defined heterostructure is an effective strategy to further enhance the photocatalytic activity of

* Corresponding author.

E-mail addresses: wuyuqicas@163.com, wuyuqi@licp.cas.cn (Y. Wu).

¹ These authors contributed equally.

the NaTaO₃-based heterojunction materials. Prof. Guan developed a synchronous etching-epitaxial growth approach for the fabrication of facet-coupling NaTaO₃/Ta₂O₅ heterostructure nanofibers, where the NaTaO₃ nanocubes in-situ grow epitaxially along [121] on the crystal plane (110) of electrospun Ta₂O₅ nanofibers. The as-prepared bare NaTaO₃/Ta₂O₅ nanofibers exhibited a photocatalytic activity for hydrogen production as high as 1579 $\mu\text{mol h}^{-1} \text{g}^{-1}$, far more than those of the corresponding Ta₂O₅, NaTaO₃ or the conventional heterostructure counterparts [18]. The excellent photocatalytic performance originated from the well-defined heterostructure which is in favor of the rapid transferring of photo-induced electrons.

In addition, the double-perovskite compound Sr₂FeTaO₆ has been proved to be an efficient visible-light photocatalyst [19]. What is more, NaTaO₃ and Sr₂FeTaO₆ all contains Ta atom, therefore, the combination of NaTaO₃ with Sr₂FeTaO₆ semiconductor by constructing well-defined heterostructure is a good strategy to improve the visible light absorption capability and photo-generated charge separation, and further enhance the photocatalytic performance of NaTaO₃ under visible light irradiation. In view of this, we have developed a modified hydrothermal approach for the fabrication of Sr₂FeTaO₆/NaTaO₃ heterojunctions sharing the same boundary Ta/Fe atom with a good photocatalytic activity. Firstly, the NaTaO₃ nanosheets were fabricated by hydrothermal method, and then, the as-synthesized NaTaO₃ nanosheets were used as self-sacrificed through an in situ hydrothermal reaction route by varying hydrothermal reaction temperature and time. The nanosized NaTaO₃ transformed gradually into Sr₂FeTaO₆ with an increase of reaction time. The phase transformation process, visible-light absorption properties, interfacial charge transfer efficiency, and photocatalytic performances of the as-prepared heterojunctions were comprehensively investigated. These results in this work will provide some of new insights into the heterojunction materials.

2. Experimental sections

2.1. Materials and reagents

All chemical reagents in our experiments were purchased from J&K Scientific Ltd and used without further purification.

2.2. Photocatalyst preparation

The samples were prepared following the procedures with some modification reported in the literature [20]. The synthesis process in detail was as following:

2.2.1. Preparation of fresh Sr(OH)₂ power

a given amount of Sr(CO₃)₂ powders dissolved into excess HNO₃ solution, and then excess NaOH powders added. After stirring for 1 h, the gained precipitates were centrifuged, and washed with the deionized water until the pH of supernate at 7.0 and dried at 80 °C for using in the next step.

2.2.2. Preparation of nanosized NaTaO₃, Sr₂FeTaO₆/NaTaO₃, and Sr₂FeTaO₆

Fe₂O₃ (1 g), fresh Sr(OH)₂ (1 g), and Ta₂O₅ (3.62 g) powders were added into 30 mL aqueous NaOH solution (4.0 mol L⁻¹), stirring vigorously for 1 h, and then transferring the mixture into a Hastelloy alloy autoclave (50 mL capacity). The autoclave was kept at 260 °C for 48 h and then cooled to room temperature naturally. The resulting precipitates were collected by centrifugation at 10,000 rpm, and further washed with the nitric acid solution (30%), sodium hydrate solution (1.0 mol L⁻¹), and deionized water thoroughly for removing the unreacted species (Fe₂O₃, Sr(OH)₂, Na⁺ ion, etc.), and then dried at 80 °C in an oven. The obtained sample was denoted as S260-48 (pure NaTaO₃ nanosheets). With the same processes, the autoclaves were firstly kept at 260 °C for 48 h, and then kept at 300 °C for 8, 16, 32, and 48 h,

respectively, and the obtained samples were denoted as S300-8, S300-16, S300-32 (Sr₂FeTaO₆/NaTaO₃ heterojunctions), and S300-48 (pure Sr₂FeTaO₆ nanoparticles), respectively.

2.2.3. Deposition of Pt cocatalyst

For photocatalytic hydrogen evolution, the 0.5 wt % Pt was deposited by conventional impregnation and subsequent H₂ reduction. Typically, the as-prepared sample (0.2 g) was immersed in 10 mL aqueous H₂PtCl₆ solution, and stirred for 24 h under dark. And then, the suspensions were completely evaporated with infrared light irradiation under the stirring condition, the gained powders were collected and reduced at 473 K for 1 h under a flow of 5% H₂/Ar (200 mL min⁻¹), denoted as Pt/S260-8, Pt/S300-8, Pt/S300-16, Pt/S300-32, and Pt/S300-48, respectively.

2.3. Characterization

The morphology, phase structure and composition of the as-prepared materials were obtained by various characterization techniques. Transmission electron microscopy (TEM) images and high-resolution TEM (HRTEM) images were obtained using a field-emission TEM (JEOL JEM-2100 F). The X-ray diffraction (XRD) patterns were recorded on a Rigaku B/Max-RB X-ray diffractometer with a nickel filtrated Cu Ka radiation. The chemical state was obtained from the X-ray photoelectron spectroscopy (XPS) measurement using a VG Scientific ESCALAB250-XPS photoelectron spectrometer with an Mg (Ka) X-ray resource (The Binding Energy scale was calibrated to 285.0 eV for the main C1s peak). The specific surface area was determined with the Brunauere-Emmette-Teller (BET) equation at 77 K by using an adsorption apparatus (Micromeritics ASAP 2020 M). Photoluminescence spectra (PL) were determined by a FluoroMax-4 Steady-Transient State Fluorescence Spectrometer. Nano LED diode emitting pulses at 460 nm with 1 MHz repetition rate and pulse duration of 1.3 ns was used as an excitation source. The electron spin resonance (ESR) signals of radicals spin-trapped by spin-trap reagent DMPO (J&K Scientific Ltd.) in water or methanol were examined on a Bruker model ESR JES-FA200 spectrometer. The element contents of samples was also obtained by using Inductively Coupled Plasma(ICP)–Mass Spectrometer (Perkin Elmer, NexION 300X). UV–vis DRS spectra were obtained on a HITACHI U-3310 spectrophotometer equipped with an integrating sphere accessory (BaSO₄ was used as a reference). The band-gap (E_g) of the as-prepared sample was calculated by Kubelka–Munk function equation, as following:

$$(\alpha h\nu)^n = A(h\nu - E_g)$$

Where α , $h\nu$, A , and E_g are the optical absorption coefficient, photonic energy, constant, and bandgap energy, respectively.

2.4. Time-resolved microwave conductivity (TRMC) measurement

The method was used to study the dynamics of photo-generated charge carriers under UV and visible light irradiation. The TRMC method is based on the measurement of the change of the microwave power reflected by a sample induced by laser pulsed illumination of samples [21,22]. For semiconductor sample, the TRMC signal ($\Delta P(t)/P$ or $I(t)$) is called (microwave) photoconductivity, it allows to follow directly, on the 10⁻⁹–10⁻³ s time scale, the decay of the number of the electrons and holes after the laser pulse by recombination or trapping of the charge-carriers. Its relative change is caused by the variation $\Delta\sigma(t)$ of the sample conductivity induced by the laser. The relationship between them has been established as following:

$$\frac{\Delta P(t)}{P} = A\Delta\sigma(t) = Ae(\Delta n(t)\mu_n + \Delta p(t)\mu_h)$$

$\Delta n(t)$ is the number of excess electrons, μ_n is the mobility of electrons, $\Delta p(t)$ and μ_h are the corresponding properties of holes. A is

independent of time, but dependent on the microwave frequency and the conductivity of sample. In this study, the incident microwaves are generated by a Gunn diode carried out at 31.4 GHz. The reflected microwaves are detected by a Schottky diode. The signal is amplified and displayed on the digitizer. Pulsed light source is an Nd:YAG laser giving an IR radiation at $\lambda = 1064$ nm with a 10 Hz frequency. Full width at half-maximum of one pulse is 10 ns. The wavelengths of 266 and 450 nm were used, and the corresponding laser energies were 1.3 and 6.0 mJ cm^{-2} , respectively.

2.5. Photocatalytic NO removal experiments

Photocatalytic activities of as-obtained samples were evaluated by NO removal (500 ppb, the lowest level making our body uncomfortable) at the ambient conditions in the successive flow reactor in a cylindrical reactor. The reactor was irradiated with a 300 W Xe lamp (PLS-SXE300, Perfect Light, Beijing, China), which is equipped with a cutoff filter ($\lambda \geq 420$ nm). In a typical procedure, 100 mg of catalyst was ultrasonically dispersed in water, and then the aqueous suspension was deposited onto the sheet glass ($4 \text{ cm} \times 6 \text{ cm}$), and finally dried at 80°C . After that, the sheet glass was placed in the middle of the reactor. The NO gas is supplied by a compressed gas cylinder with a concentration of 500 ppb (N_2 balance). The desired relative humidity level in NO flow was controlled at 50% through a humidification chamber driven by the cleaned and compressed air. The gas streams were completely premixed by a gas blender, and the flow rate was at 1 L min^{-1} by a mass flow controller. For all experiments, light irradiation was started after the adsorption-desorption balance. The effluent concentrations of NO and NO_x ($\text{NO} + \text{NO}_2$) were continuously measured using a Chemiluminescence Detector. The specific concentration was collected on NO analyzer (Teledyne, NO_x analyzer, model 42i), and the NO_2 concentration was determined by the concentration difference between NO_x and NO. The NO removal percentage η (%) was obtained by following equation:

$$\eta = \frac{C_0 - C_t}{C_0}$$

Where C_0 is the initial concentration of NO in ppb level, and C_t is the varied concentration NO at a given irradiation time t in ppb level.

2.6. Photocatalytic hydrogen production experiments

The photocatalytic activity tests were carried out at room temperature. Photocatalytic hydrogen evolution experiments were performed in a 190 mL quartz flask with a flat window. The reactor was sealed with a silicone rubber septum for sampling. A 300 W Xenon lamp equipped with a 420 nm cutoff filter was used as a light source. The reactant mixture was gained by ultrasonically dispersing 100 mg of powder photocatalyst in 100 mL of aqueous triethanolamine (TEOA, 15 vol%, pH 7) solution, and then purged with argon gas for 40 min before irradiation. During the photocatalytic process, 0.5 mL gas sample in the top of reactor was collected intermittently through the septum and the amount of hydrogen evolution was measured with gas chromatography (Agilent 6820, TCD, 13X Column, Ar carrier).

The apparent quantum efficiency (AQE) was measured under the same photocatalytic reaction conditions with irradiation light through a bandpass filter (420, 450, 500, 500, and 600 nm). Photon flux of the incident light was determined using Newport 2936-R optical power meter. The following equation was used to calculate the AQE:

$$\text{AQE} = \frac{2 \times \text{the number of evolved hydrogen molecules}}{\text{the number of incident photons}} \times 100\%$$

2.7. Working electrode preparation and photoelectrochemical experiments

Photocurrent responses of photocatalyst samples were measured

using an electrochemical analyzer (CHI660E) in a homemade standard three-compartment cell. Platinum foil was used as the counter electrode, and Ag/AgCl electrode used as the reference electrode. The working electrode was prepared as following: the catalyst ink was first prepared by ultrasonically dispersing 4 mg of catalyst material and 80 μL of 5 wt % nafion solution in 2 mL of H_2O . Then 400 μL of catalyst ink dispersions were drop-coated directly onto FTO glass surface (ca. 2.0 cm^2) by microsyringe and dried under an infrared heat lamp. The geometrical surface areas of working electrode exposed to the electrolyte was a circular-film of 1.0 cm^2 . TEOA solution (15 vol%, pH 7) was used as supporting electrolyte. A 300 W xenon lamp with optical cutoff filter ($\lambda \geq 420$ nm) was used for excitation light.

2.8. Detection of intermediate active species

Hydroxyl radicals ($\cdot\text{OH}$), superoxide radical anions ($\text{O}_2^{\cdot-}$), and electron/holes (e^-/h^+) are the main active species involved in the photocatalytic processes. To determine and reveal the role of these intermediates and reaction mechanism, a series of scavenger test experiments were conducted. Herein, isopropyl alcohol (IPA), potassium iodide (KI), *p*-benzoquinone (PBQ), and AgNO_3 were used as $\cdot\text{OH}$, h^+ , $\text{O}_2^{\cdot-}$, and e^- scavengers, respectively. The detailed quenching test process was carried out as following: Firstly, 100 mg of catalyst was deposited onto the sheet glass as described in Section 2.5, and then 2 ml of aqueous solution contained 10 mg of scavenger was dropped onto the as-prepared sheet glass. Finally, after natural air drying, the as-prepared sheet glass was placed in the middle of the reactor for the quenching test.

3. Results and discussions

3.1. Structure and composition characterizations

XRD technique was adopted to verify the phase of as-synthesized samples and further analyze the corresponding phase transformation procedure during the hydrothermal process. Fig. 1 shows the XRD patterns of as-synthesized samples. As shown in Fig. 1A, for sample S260-48, all the diffraction peaks in XRD pattern can be indexed to the monoclinic NaTaO_3 (JCPDS No.74-2481). No additional diffraction peaks belonging to other phases are observed, suggesting that sample S260-48 is pure NaTaO_3 . Similarly, sample S300-48 is proved to be pure $\text{Sr}_2\text{FeTaO}_6$, and all observed diffraction peaks correspond to the orthorhombic $\text{Sr}_2\text{FeTaO}_6$ (JCPDS No.88-0135). As for sample S300-8, S300-16, and S300-32, diffraction peaks belonging to monoclinic NaTaO_3 and orthorhombic $\text{Sr}_2\text{FeTaO}_6$ mentioned above all could be observed, illustrating that sample S300-8, S300-16, and S300-32 all display the coexistences of both NaTaO_3 and $\text{Sr}_2\text{FeTaO}_6$, the result of which resembles to that of literature [23]. No peaks belonging to additional impurity phases are detected in the diffraction patterns, therefore, we can consider that during hydrothermal reaction process, there are no other appreciable chemical reactions proceeding between NaTaO_3 and $\text{Sr}_2\text{FeTaO}_6$. Furthermore, the peak intensity assigned to $\text{Sr}_2\text{FeTaO}_6$ phase becomes stronger with prolonging the reaction time as shown in Fig. 1B, indicating that the NaTaO_3 phase is gradually transformed into $\text{Sr}_2\text{FeTaO}_6$ phase. The phase composition of sample S300-8, S300-16, and S300-32 were calculated based on adiabatic method and the corresponding formula was presented as following:

$$W_x = \frac{I_{xi}}{K_A^x \sum_{i=A}^N \frac{I_i}{K_A^i}}$$

Where W_x was the weight fraction of x component. I_{xi} was the diffraction peak intensity of x component; K was the intensity factor. For sample S300-8, S300-16, and S300-32, the weight fraction of $\text{Sr}_2\text{FeTaO}_6$ is 16.4, 55.0, and 64.5 wt%, respectively, increasing as the reaction time prolonging, and the corresponding molar ratio of $\text{Sr}_2\text{FeTaO}_6$ to

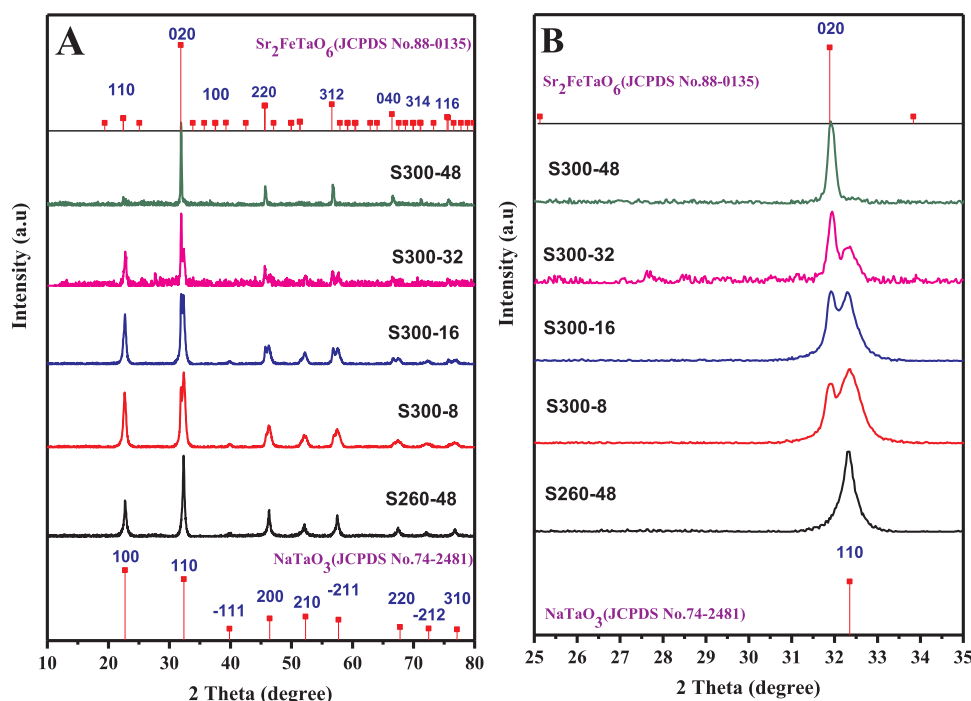


Fig. 1. XRD patterns of pure NaTaO_3 (S260-48), pure $\text{Sr}_2\text{FeTaO}_6$ (S300-48), and $\text{Sr}_2\text{FeTaO}_6/\text{NaTaO}_3$ heterojunctions (S300-8, S300-16, S300-32).

NaTaO_3 is 0.19, 0.85, and 1.82, respectively. All the above XRD results reveal that, by adjusting the hydrothermal temperature and reaction time, the $\text{Sr}_2\text{FeTaO}_6/\text{NaTaO}_3$ heterojunctions can be obtained, and the phase composition can be controlled as well.

The morphology, phase structure, and heterojunction feature of as-prepared samples are studied by TEM and HRTEM. As shown in Fig. 2A, the pure NaTaO_3 (sample S260-48) has a nanosheet structure, and the lattice fringes with the d spacing of 0.282 nm match well with the (110) crystalline plane of NaTaO_3 . Fig. 2E shows that the prepared pure $\text{Sr}_2\text{FeTaO}_6$ (sample S300-48) is nanoparticle with a diameter of about 25–50 nm, which is different from the previously reported results [19]. As far as we know, this is the first report for nanoscale $\text{Sr}_2\text{FeTaO}_6$ particles, as a result, it can supply more active sites for photocatalytic reaction and what is more important it can supply more dangling bonds which can be used to forming interfacial bonding when constructing semiconductor/ $\text{Sr}_2\text{FeTaO}_6$ heterojunctions. The atomic-scale intimate interfacial contact benefits the rapid separation and transferring of photo-generated charges. The lattice fringes with the d spacing of 0.227 nm in Fig. 2e correspond to the (202) crystalline plane of $\text{Sr}_2\text{FeTaO}_6$. As shown in Fig. 2B, C and D, both NaTaO_3 nanosheets and $\text{Sr}_2\text{FeTaO}_6$ nanoparticles were observed, indicating that there are two phase and morphologies coexisting in the $\text{Sr}_2\text{FeTaO}_6/\text{NaTaO}_3$ heterojunctions (S300-8, S300-16 and S300-32). The corresponding lattice fringe identification was obviously observed in the HRTEM images of sample S300-8, S300-16 and S300-32 (Fig. 2b,c and d). For the $\text{Sr}_2\text{FeTaO}_6/\text{NaTaO}_3$ heterojunction, the lattice fringe of sample S300-8 with the d spacing of 0.278 nm corresponds to the (110) crystalline plane of NaTaO_3 , whereas the lattice fringes with the d spacing of 0.224 nm matches with the (202) crystalline plane of $\text{Sr}_2\text{FeTaO}_6$. The similar results could be observed from the others $\text{Sr}_2\text{FeTaO}_6/\text{NaTaO}_3$ heterojunctions (sample S300-16 and S300-32). More importantly, there is an obvious transitional zone (the lattice is twisted and disordered) with a certain space between phase $\text{Sr}_2\text{FeTaO}_6$ (202) and NaTaO_3 (110), abbreviated to S, as shown in Fig. 2b, c and d, which are marked with yellow dashed line. It is interesting that, S, the space of the transitional zone of the $\text{Sr}_2\text{FeTaO}_6/\text{NaTaO}_3$ heterojunctions (sample S300-8, S300-16 and S300-32) will be expanded with the prolonged reaction time, and the average S value is about 0.25, 0.35, and 0.45 nm,

respectively. It infers that the space of the transitional zone of the heterojunctions is controllable in atomic level by adjusting the prepared condition.

The XPS analysis was carried out to study the surface chemical compositions and states. All binding energies are corrected by the C 1s signal at 284.8 eV, and shown in Fig. 3 and Table 1. Fig. 3a displays the survey spectra of various samples. It clearly shows that sample S260-48 is mainly composed of Na, Ta, and O elements without Sr, Fe or other impurities, excluding adventitious carbon-based contaminant. Similarly, sample S300-8, S300-16, and S300-32 are mainly composed of Na, Sr, Fe, Ta, and O elements and sample S300-48 is mainly composed of Sr, Fe, Ta, and O elements. Fig. 3c reveals the high-resolution XPS spectra of Sr 3d for all samples. Except for sample S260-48, there are two strong peaks observed for sample S300-8, S300-16, S300-32, and S300-48. The binding energies of these two peaks are 134.25 and 132.44 eV in sample S300-8, which are assigned to Sr 3d_{3/2} and Sr 3d_{5/2}, respectively. The binding energy is smaller than that reported for $\text{Sr}_2\text{Ta}_2\text{O}_7$ having oxidation states of Sr^{2+} [24]. The shift of binding energy originated from the changes of local chemical environment, which probably resulted from the introduction of Fe atom in $\text{Sr}_2\text{FeTaO}_6$ and the formation of an intimate interfacial structure between NaTaO_3 and $\text{Sr}_2\text{FeTaO}_6$. The Ta 4f spectrum of sample S260-48 in Fig. 3e display two primary bands at 25.87 and 27.73 eV, indicating a characteristic of Ta^{5+} in NaTaO_3 [25]. The Ta 4f_{7/2} binding energy of sample S300-48 is 24.83 eV, which is also smaller than that of $\text{Sr}_2\text{Ta}_2\text{O}_7$ and NaTaO_3 [26]. Furthermore, the Ta 4f_{7/2} binding energies of sample S300-8, S300-16, and S300-32 are decreased in turn in the range of 25.87–24.83 eV. The spectra of Fe 2p in Fig. 3d present two major peaks with binding energies located at 711.73 and 725.03 eV, which are ascribed to the Fe 2p_{3/2} and Fe 2p_{1/2}, consistent with those reported for $(\text{Sr}_{1-x}\text{La}_x)_2\text{FeTaO}_6$ having oxidation state of Fe^{3+} [27]. The XPS spectra of O 1s are shown in Fig. 3f. It is observed that the O1s peak located at 530.21 eV of sample S260-48 could be attributed to the oxygen in NaTaO_3 host matrix. For sample S300-48, the peak at 529.8 eV is attributed to the lattice Ta-O-Fe in the $\text{Sr}_2\text{FeTaO}_6$. Furthermore, there are two types oxygen atom existing in sample S300-8, S300-16, and S300-32, indicating that both NaTaO_3 and $\text{Sr}_2\text{FeTaO}_6$ coexist in the $\text{Sr}_2\text{FeTaO}_6/\text{NaTaO}_3$ heterojunctions, which is in accordance with the results of XRD

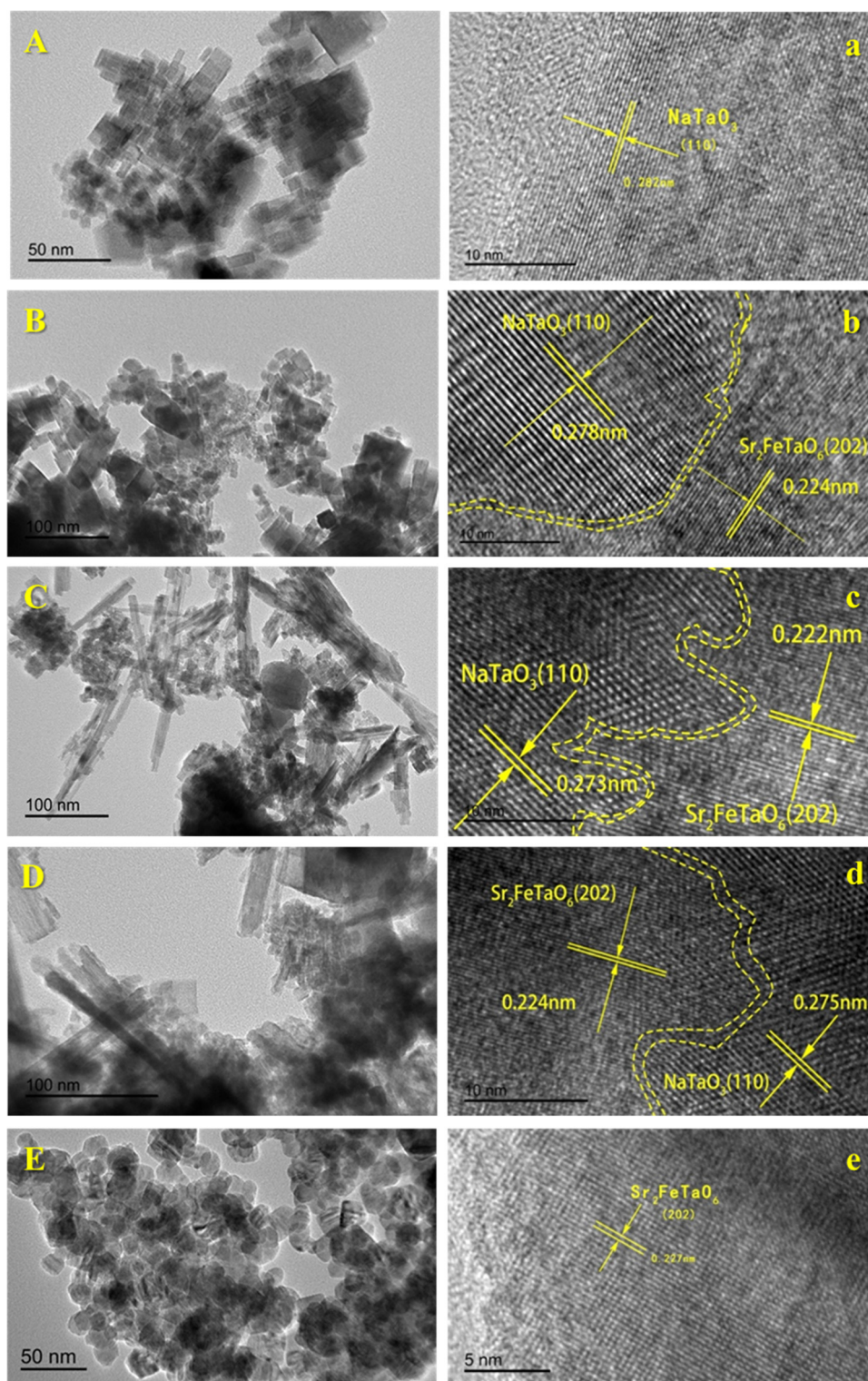


Fig. 2. TEM and HREM images of pure NaTaO_3 (S260-48: A, a), $\text{Sr}_2\text{FeTaO}_6/\text{NaTaO}_3$ heterojunctions (S300-8: B, b; S300-16: C, c; S300-32: D, d), and pure $\text{Sr}_2\text{FeTaO}_6$ (S300-48: E, e).

and TEM analysis. What should be mentioned that the systematic shift of the binding energy for lattice oxygen is probably related to the local environmental variation, which resulted from the phase transformation from NaTaO_3 to $\text{Sr}_2\text{FeTaO}_6$, being similar to the results observed for the orbital Ta 4f and Fe 2p. Moreover, all samples exhibit a peak at about 531.2 eV, which is the characteristic peak of chemisorbed H_2O or OH^- on the surface [28].

In addition, XPS characterization can give atomic percent of Na, Sr, Fe, Ta and O atoms in sample S260-48, S300-8, S300-16, S300-32, and S300-48. The atomic ratios normalized by Ta atomic content were listed in Table 2. The molar ratio from XPS of $\text{Sr}_2\text{FeTaO}_6$ to NaTaO_3 , i.e. the atomic ratio of Fe/Na, in sample S300-8, S300-16, and S300-32 is 0.17, 0.61, and 1.41, respectively, which is not exactly line with the result from the XRD calculation listed in Table 2. The reasonable explanation

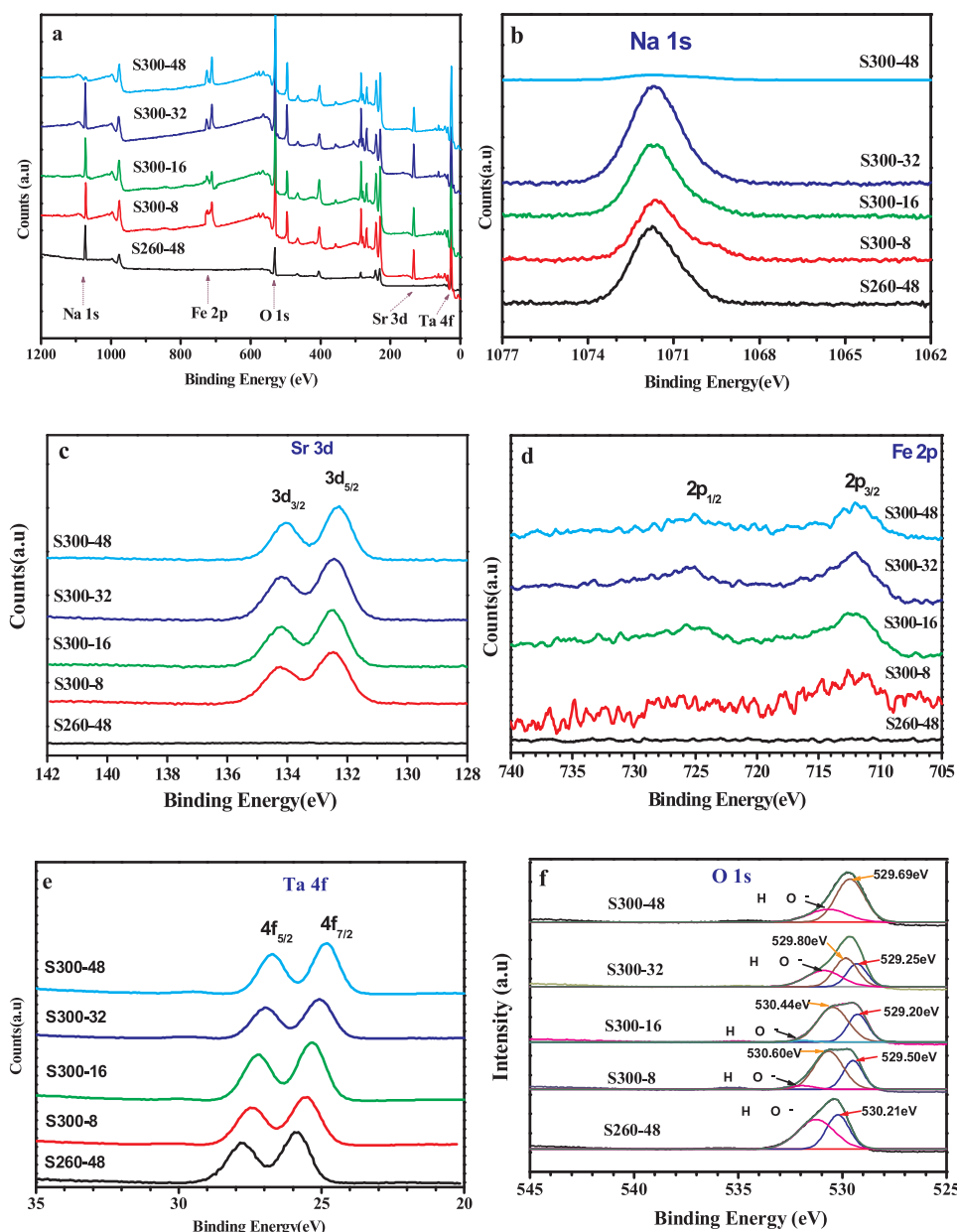


Fig. 3. XPS spectra of pure NaTaO_3 (S260-48), $\text{Sr}_2\text{FeTaO}_6/\text{NaTaO}_3$ heterojunctions (S300-8, S300-16, S300-32), and pure $\text{Sr}_2\text{FeTaO}_6$ (S300-48): (a) survey scan, (b) Na 1s, (c) Sr 3d, (d) Fe 2p, (e) Ta 4f, and (f) O 1s.

could be gained from a fact that the composition content of XPS semi-quantitative analysis originates from the shallow surface ca. 1–2 nm of the samples. The molar ratio from XRD data originates from the bulk of the samples, but it would be affected by the crystallinity of component.

And so, the convincing molar ratio was further confirmed by inductively coupled plasma resonance (ICP) spectroscopy measurement, as shown in Table 2. The molar ratio of $\text{Sr}_2\text{FeTaO}_6$ to NaTaO_3 from ICP in sample S300-8, S300-16, and S300-32 is 0.18, 0.53, and 1.17,

Table 1
Binding Energies (eV) of various samples from XPS analysis.

Samples	Binding Energy (eV)								
	Na 1s	Sr 3d		Fe 2p		Ta 4f		O1s	
		3d _{3/2}	3d _{5/2}	2p _{1/2}	2p _{3/2}	4f _{5/2}	4f _{7/2}	NaTaO ₃	Sr ₂ FeTaO ₆
S260-48	1071.77	/	/	/	/	27.73	25.87	530.21	/
S300-8	1071.62	134.24	132.52	725.85	712.56	27.41	25.54	529.50	530.60
S300-16	1071.64	134.21	132.50	725.45	712.19	27.16	25.31	529.22	530.44
S300-32	1071.63	134.14	132.40	725.23	711.99	26.87	25.01	529.23	529.80
S300-48	/	133.97	132.25	725.22	711.94	26.69	24.83	/	529.69

Table 2

Atomic ratio of various samples from XPS and ICP, and Fe/Na atomic ratio from ICP, XPS, and XRD.

Samples	Atomic ratio from XPS ^a					Atomic ratio from ICP ^a				Atomic ratio of Fe/Na ^b		
	Na	Sr	Fe	Ta	O	Na	Sr	Fe	Ta	ICP	XPS	XRD
S260-48	1.17	/	/	1	3.18	1.02	/	/	1	/	/	/
S300-8	0.95	0.56	0.16	1	3.14	0.84	0.32	0.15	1	0.18	0.17	0.19
S300-16	0.75	1.07	0.45	1	3.90	0.66	0.69	0.35	1	0.53	0.61	0.85
S300-32	0.53	1.54	0.74	1	6.01	0.46	1.10	0.54	1	1.17	1.41	1.82
S300-48	/	2.11	0.87	1	6.90	/	2.06	0.98	1	/	/	/

^a Normalized by Ta atomic content.^b Atomic ratio of Fe/Na used for estimating the Sr₂FeTaO₆/NaTaO₃ molar ratio.

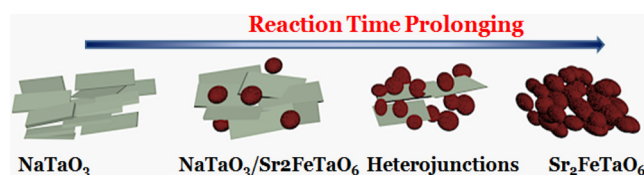
respectively.

In summary, based on the results of XRD, (HR)TEM, XPS and ICP analysis, the sample S260-48 and S300-48 are pure NaTaO₃ nanosheets and Sr₂FeTaO₆ nanoparticles, respectively, and the sample S300-8, S300-16, and S300-32 are all Sr₂FeTaO₆/NaTaO₃ heterojunctions with the molar ratio 0.18, 0.53, and 1.17, respectively. For Sr₂FeTaO₆/NaTaO₃ heterojunctions (sample S300-8, S300-16, and S300-32), it is more interesting that the space of the transitional zone of the heterojunctions, *S*, will be controllably expanded with the prolonged reaction time.

3.2. Formation mechanism of the Sr₂FeTaO₆/NaTaO₃ heterojunction

According to the analysis mentioned above and previous literature [23], the synthesis strategy was self-sacrifice, and the formation progress was proposed as following: when the reaction temperature was controlled at 260 °C, the raw materials of NaOH and Ta₂O₅ reacted forming NaTaO₃ nanosheets, and Sr(OH)₂ and Fe₂O₃ acted only as the structure-guiding agent, like NaCl to β-Fe₂O₃ [29]. When the hydrothermal temperature rose to 300 °C, the Sr(OH)₂ and Fe₂O₃ reacted simultaneously with NaTaO₃ forming Sr₂FeTaO₆ nanoparticles by consuming NaTaO₃. With the hydrothermal time increasing, the NaTaO₃ nanosheets were gradually transformed into Sr₂FeTaO₆ nanoparticles. As a result, the content of NaTaO₃ decreased, and the content of Sr₂FeTaO₆ increased until the NaTaO₃ phase transformed completely into Sr₂FeTaO₆, as shown in Scheme 1.

In order to verification the above conjecture, the Sr(OH)₂ content was quantitative analyzed after hydrothermal reaction for 48 h at 260 °C. In brief, after hydrothermal reaction finishing, the raw product was first washed with boiling water, and then the supernate was collected after centrifugation (The Sr(OH)₂ was easily soluble in boiling water). Next, 100 mL Na₂CO₃ solution (0.5 mol L⁻¹) was added into it, stirring for 24 h; finally, the precipitate was centrifuged and dried at 60 °C. The weight of obtained SrCO₃ was 1.16 g, which was equal to 0.948 g Sr(OH)₂. Taking into account the experimental error, we believed the Sr(OH)₂ did not participate in hydrothermal reaction. Meanwhile, the centrifugal sediment washed with nitric acid solution (30%), and then the supernate was collected after centrifugation. Next, 100 mL NaOH solution (1.0 mol L⁻¹) was added into it, stirring for 24 h; finally, the precipitate was centrifuged and dried under vacuum at 60 °C. The weight of obtained Fe(OH)₃ was 0.65 g, which was equal to 0.97 g Fe₂O₃. Taking into account the experimental error, we also believed the Fe₂O₃ did not participate in hydrothermal reaction.



Scheme 1. Schematic illustrating the synthesis of NaTaO₃/Sr₂FeTaO₆ heterojunctions.

Furthermore, we repeated above hydrothermal process without Sr(OH)₂, the as-obtained NaTaO₃ was nanoparticles, as shown in Fig. 4a and b. The result of XRD characterization state clearly that NaTaO₃ was also can be synthesized without Sr(OH)₂, but the as-obtained NaTaO₃ were irregular nanoparticles, which proved that the Sr(OH)₂ species probably was the structure-guiding agent for the synthesis of NaTaO₃ nanosheets.

3.3. Photocatalyst performances

The photocatalytic activities of the as-prepared samples were evaluated for the degradation of NO and photocatalytic water splitting for hydrogen evolution under visible irradiation ($\lambda \geq 420$ nm), as shown in Fig. 5. For comparison, the mixture of Sr₂FeTaO₆ and NaTaO₃ with the same molar ratio as the sample S300-16 was prepared by mechanical mixing and denoted as S-MIXT. Fig. 5a gives the NO concentration (*C*/*C*₀) against irradiation time over sample S260-48, S300-8, S300-16, S300-32, S300-48, and S-MIXT under visible-light irradiation. Under visible light irradiation for 40 min, the pure NaTaO₃ (S260-48) does not exhibit any photocatalytic activity for NO removal because of its large bandgap. The NO removal ratio, η (%), of the pure Sr₂FeTaO₆ (S300-48) is only about 52%. The poor photocatalytic ability is caused by various intrinsic properties of itself, for example, the fast recombination of e^- – h^+ pairs. After irradiation for 40 min, the η of the Sr₂FeTaO₆/NaTaO₃ heterojunctions (S300-8, S300-16, and S300-32) are 40, 72, and 59%, respectively, indicating that for the heterojunctions composed of wide and narrow bandgap component, the molar ratio has played an important factor on the visible-light-driven photocatalytic activity because the visible-light-absorbability varied with the molar ratio changed. The optimum molar ratio for Sr₂FeTaO₆/NaTaO₃ heterojunction is 0.53 in this photocatalytic system. The η of sample S-MIXT is 51%, lower than that of S300-16 heterojunction, indicating that the interfacial structure of heterojunction should be more conducive to electron transport, thereby enhancing the photocatalytic oxidation activity.

Furthermore, the photocatalytic reduction performances were evaluated by monitoring their hydrogen production in the presence of sacrificial agent under light irradiation. Here, loaded Pt (0.5 wt%) and aqueous TEOA solution (15 vol%) are respectively used as the cocatalyst and hole scavenger to promote photo-reduction reactions. The result is presented in Fig. 5b. Under visible light irradiation, no hydrogen was detected for pure NaTaO₃ (sample 260-48), but for the Sr₂FeTaO₆/NaTaO₃ heterojunctions (sample S300-8, S300-16, and S300-32) and pure Sr₂FeTaO₆ (S300-48), hydrogen evolution is immediately detected. The sample S300-16 exhibits the highest photocatalytic activity with 667 μ mol hydrogen amount in 5 h irradiation period (i.e. 1334 μ mol h⁻¹ g⁻¹), much higher than those of sample S300-8, S300-32, and S300-48, with the hydrogen amount 332, 452, and 360 μ mol, respectively (i.e. 664, 904, and 720 μ mol h⁻¹ g⁻¹, respectively). In contrast, photocatalytic hydrogen production of sample S-MIXT in 5 h is 382 μ mol (764 μ mol h⁻¹ g⁻¹), about 43% lower than that of sample S300-16 heterojunction. Obviously, such an improvement over photocatalytic activity arises from the special interfacial structure of sample

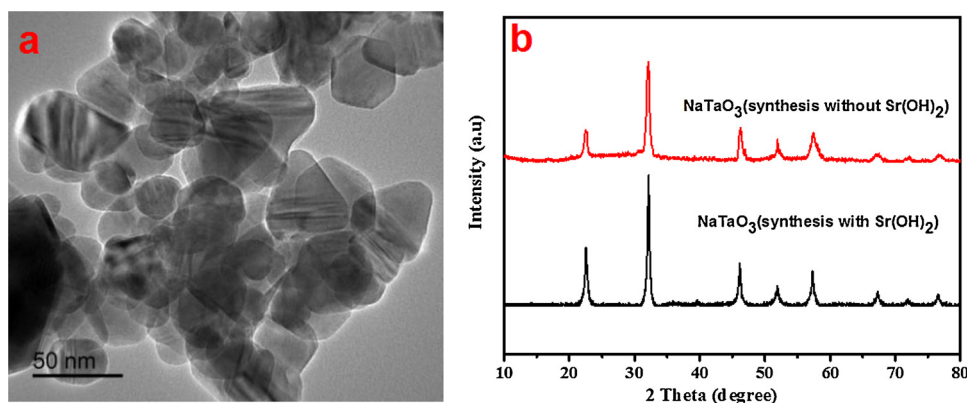


Fig. 4. TEM image (a) and XRD pattern(b) of pure NaTaO_3 obtained with and without $\text{Sr}(\text{OH})_2$.

S300-16 heterojunction which is conducive for the rapid photo-induced electron transferring.

Fig. 6 shows the wavelength dependence of the apparent quantum efficiency (AQE) for hydrogen generation on sample S260-48, S300-16 and S300-48 under visible light at TEOA solution. For S260-48, all the AQE at 420, 450, 500, 550, and 600 nm was zero, in consistent with the result of photocatalytic activity. For S300-16, a maximum AQE of 38.8% is achieved at 420 nm and then gradually decreases to 24.9% at 450 nm, 10.1% at 500 nm, 2.3% at 550 nm and 0.88% at 600 nm. Compared with S300-16, the AQE of S300-48 was smaller under the same conditions. The result indicated that S300-48 was a visible-light-driven photocatalyst and the interfacial heterojunction was in favor of the rapid transferring of photo-induced electrons. In addition, the stability test results were presented in Fig. 7a, b, and c, the photocatalytic hydrogen production activity after six cycles of Pt-loaded S300-16 maintained 93% of its initial activity, and the photocatalytic NO removal ratio within 100 h of S300-16 maintained in a relative stable value, indicating the photocatalyst structure didn't have obvious changes before and after long-term photocatalytic reaction, and exhibiting excellent photo-stability of photocatalytic activity. Based on the above results, we have reasons to believe that the in-situ hydrothermal fabrication of $\text{Sr}_2\text{FeTaO}_6/\text{NaTaO}_3$ heterojunction could efficiently promote the photocatalytic performances whether hydrogen evolution or NO removal. What roles do the $\text{Sr}_2\text{FeTaO}_6/\text{NaTaO}_3$ heterojunctions have played in these processes? More discussion is needed as the following sections.

3.4. Roles of $\text{Sr}_2\text{FeTaO}_6/\text{NaTaO}_3$ heterojunctions in promoting the electron-hole separation and visible-light absorption

Surface area is a crucial factor for the activity of photocatalyst. Hence, the surface area (SBET) of various samples was measured by the

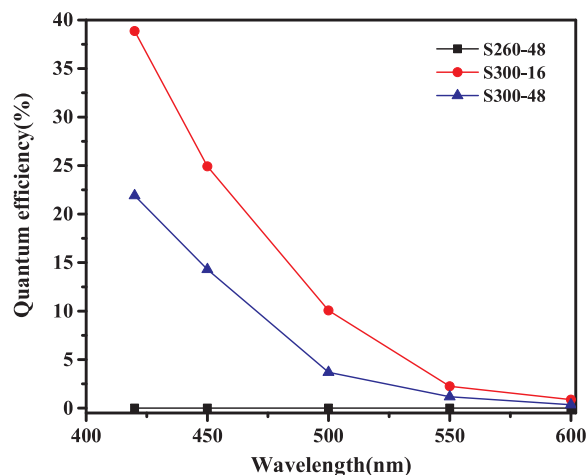


Fig. 6. The apparent quantum efficiency (AQE) for hydrogen generation on S260-48, S300-16, and S300-48 under monochromatic light irradiation ($\lambda = 420, 450, 500, 550, \text{ and } 600 \text{ nm}$).

N_2 adsorption-desorption experiments, and the results are shown in Fig. 8 and Table 3. The as-synthesized samples show the typical type-IV adsorption-desorption isotherm with type H3 hysteresis loop, which indicates the presence of porous structure formed [28]. The BET surface areas for sample S260-48, S300-8, S300-16, S300-32, and S300-48 are 37.22, 38.72, 40.97, 39.65, and $38.54 \text{ m}^2 \text{ g}^{-1}$, respectively. And so, the fabrication of $\text{Sr}_2\text{FeTaO}_6/\text{NaTaO}_3$ heterojunction has not remarkable effect on the surface area.

Further, the optical absorption characteristics of the as-prepared samples were measured by UV-Vis diffuse reflection spectroscopy and the corresponding bandgaps were also calculated. As shown in Fig. 9a,

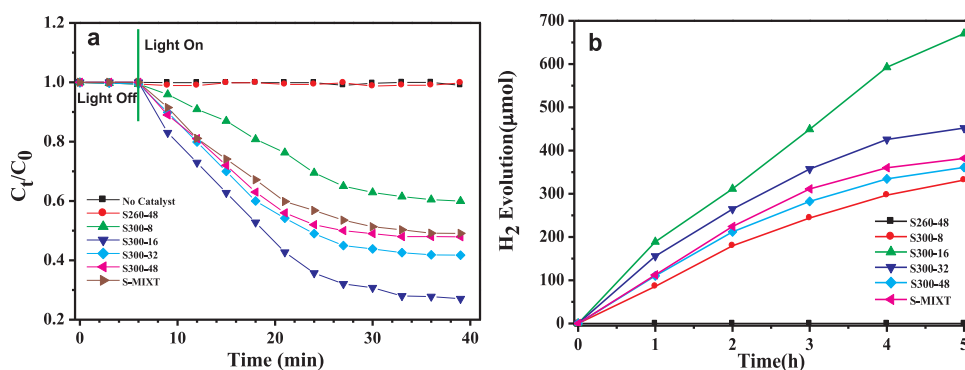


Fig. 5. Photocatalytic performances over pure NaTaO_3 (S260-48), $\text{Sr}_2\text{FeTaO}_6/\text{NaTaO}_3$ heterojunctions (S300-8, S300-16, S300-32), pure $\text{Sr}_2\text{FeTaO}_6$ (S300-48), and mechanical mixture (S-MIXT) under visible light irradiation ($\lambda \geq 420 \text{ nm}$): (a) NO oxidation (b) hydrogen production, 0.5 wt% Pt loading, TEOA solution (15 vol%).

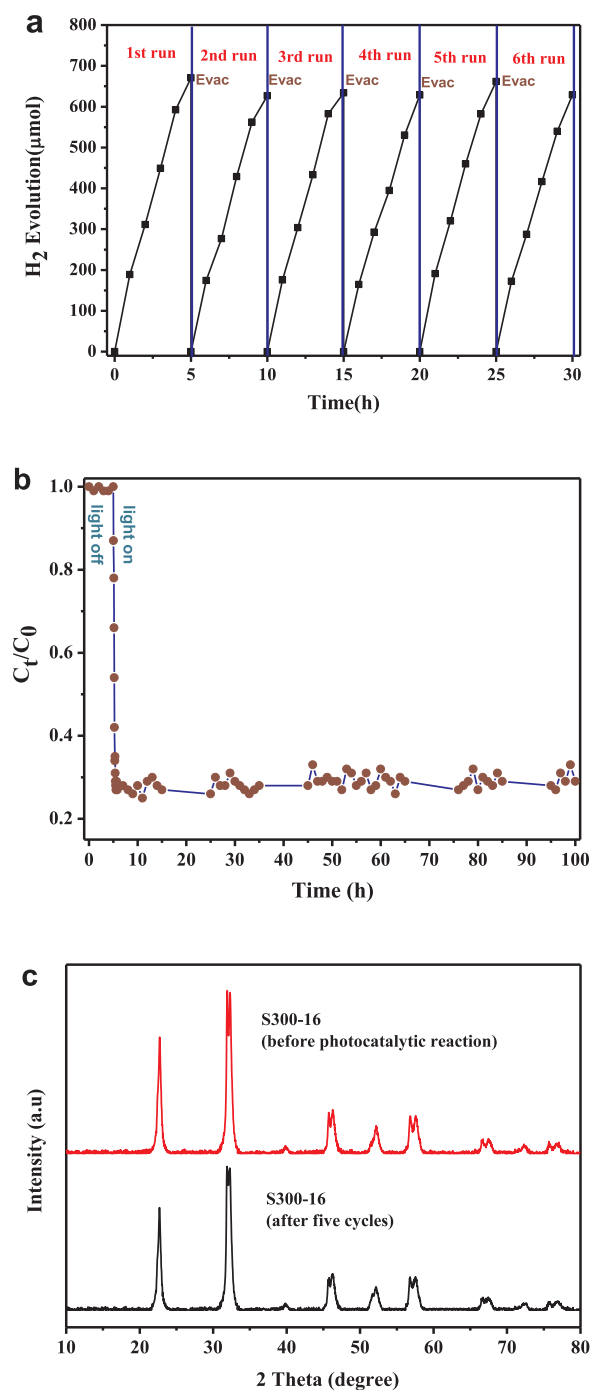


Fig. 7. Stability of sample S300-16 in photocatalytic H₂ evolution reaction (a) and NO oxidation reaction (b); XRD patterns of sample S300-16 before and after the photocatalytic reaction (c).

the maximal absorbance wavelength for sample S260-48, S300-8, S300-16, S300-32, and S300-48 is located approximately at 311, 433, 502, 523, and 602 nm, respectively, which suggests that the pure NaTaO₃ only response to the UV light, while the other samples have good absorbability in visible light region. The maximal absorbance wavelength increases gradually in the similar order of the molar ratio of Sr₂FeTaO₆ component related to the hydrothermal reaction time [30], being consistent with results of SEM and XRD. As shown in Fig. 9b, the corresponding bandgap (E_g) of sample S260-48, S300-8, S300-16, S300-32, and S300-48 is 3.98, 2.86, 2.47, 2.37, and 2.06 eV, respectively [31,32]. The bandgaps of NaTaO₃ and Sr₂FeTaO₆ are close to the previously reported values of pure NaTaO₃ [33] and Sr₂FeTaO₆ [19]. And

thus, the results from UV–Vis diffuse reflection spectroscopy indicated that the introducing narrow-bandgap Sr₂FeTaO₆ component into the Sr₂FeTaO₆/NaTaO₃ heterojunction could obviously enhance its absorbability in visible light region.

Moreover, the separating and transferring efficiency of the excited electrons and holes for the S300-16 heterojunction can be validated by photocurrent under 300 W Xenon Lamp irradiation. Higher photocurrent density originates from the enhanced transport and separation efficiency of photo-generated carriers [34]. As outlined in Fig. 10, among all the samples, the photocurrent density of sample S300-16 heterojunction is the highest, meaning that the separating and transferring efficiency of the excited electrons and holes on sample S300-16 heterojunction is the highest, which is consistent with its superior photocatalytic activity.

It is well known that the Photoluminescence (PL) emission intensity is related to the recombination of electrons and holes. The lower PL emission intensity means less opportunities for electron–hole pairs' recombination, and thereby, the more effective migration of charge-carriers [35]. Fig. 11a displays the PL spectra of the as-prepared sample S300-8, S300-16, S300-32, and S300-48 together with that of S-MIXT for comparison. All samples exhibit an emission peak from 550 ~ 700 nm. The main emission peaks are at about 583 and 640 nm. With reference to the literature [36], the band at 583 nm is attributed to a band to band transition; the band at 640 nm can be assigned to O²⁻ → Fe³⁺ transition [19]. In particular, the sample S300-16 heterojunction has the highest photocatalytic activity and the lowest PL intensity, which demonstrates that the S300-16 heterojunction has the smallest recombination efficiency of photo-induced electron–hole pairs, and the interfacial structure of sample S300-16 heterojunction is more conducive for the transfer and separation of photo-generated electron–hole pairs, resulting in the highest photocatalytic activity under visible light irradiation. Fig. 11b shows the EIS Nyquist plots of the sample S260-48, S300-8, S300-16, S300-32, S300-48 and S-MIXT with visible light ($\lambda \geq 420$ nm) irradiation. The arc radius on EIS Nyquist plot of sample S300-16 heterojunction is the smallest. Since the radius of the arc on the EIS spectra reflects the reaction rate occurring at the surface of electrode [37], a more effective separation of photo-generated electron–hole pairs and faster interfacial charge transfer occur on S300-16 heterojunction photocatalyst [38]. This result clearly indicates that the special interfacial structure between NaTaO₃ and Sr₂FeTaO₆ could effectively enhance the separation and transferring of photo-generated electron–hole pairs.

For further comparing the conduction ability of photo-generated electrons, the electronic properties of the pure NaTaO₃ (S260-48), optimal Sr₂FeTaO₆/NaTaO₃ heterojunction (S300-16), pure Sr₂FeTaO₆ (S300-48), and mechanical mixture Sr₂FeTaO₆ + NaTaO₃ (S-MIXT) were studied by TRMC technique at both UV and visible light regions, namely 266 and 450 nm, respectively, as shown in Fig. 12. The charge-carrier dynamics behavior of S300-16 heterojunctions is different to those of S260-48 and S-MIXT. TRMC signals show that, under UV excitation at 266 nm (Fig. 12a), four samples are all activated. The electrons are induced in the conduction band (CB) of S260-48, as shown by the sharp increase of TRMC signal, reaching I_{\max} values (0.28 mV). Similar condition can be seen in S300-16 heterojunction, S-MIXT, and S300-48. However, the decay of the signals is faster for S300-16 heterojunction. The TRMC signals are mainly related to the electrons which have higher mobility than holes [39]. The decrease of the TRMC signals in S300-16 is probably caused by the rapid electron transferring due to the special interfacial structure, decreasing the recombination process and resulting in a decrease in the recombination of charge carriers. This acceleration of the signal decay, with metal oxide exhibiting capacitive properties, has also been observed for the modification of TiO₂ with CuO clusters [40]. Under excitation in the visible region with wavelengths of 450 nm (as shown in Fig. 12b), there is no light absorption by pure S260-48 because of its large band gap. TRMC signal of the S300-16 heterojunction is obtained due to the narrow band

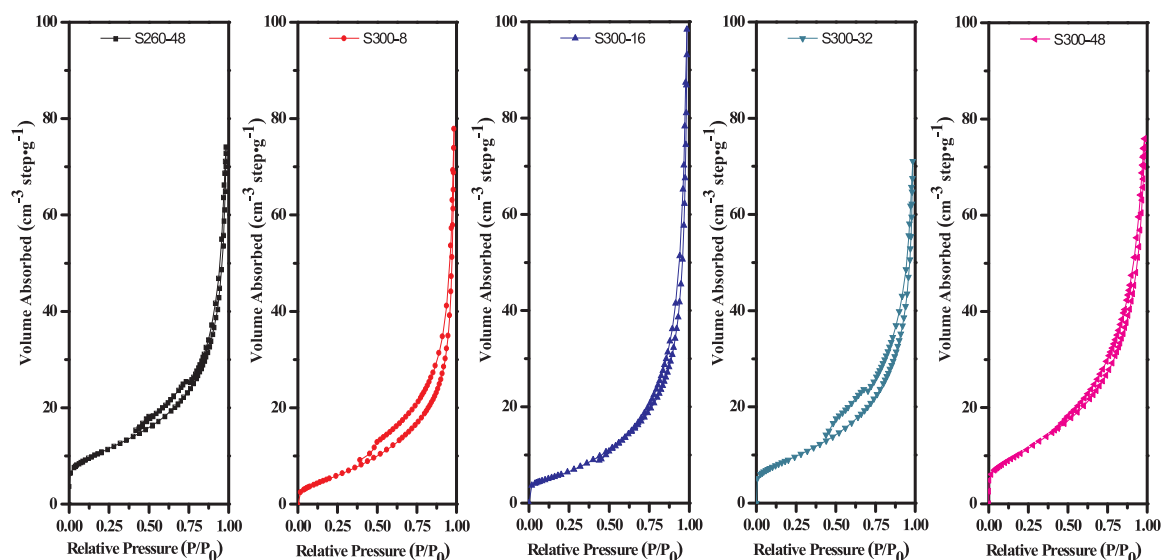


Fig. 8. N_2 adsorption-desorption isotherms of pure $NaTaO_3$ (S260-48), $Sr_2FeTaO_6/NaTaO_3$ heterojunctions (S300-8, S300-16, S300-32), and pure Sr_2FeTaO_6 (S300-48).

Table 3

BET surface areas of pure $NaTaO_3$ (S260-48), $Sr_2FeTaO_6/NaTaO_3$ heterojunctions (S300-8, S300-16, S300-32), and pure Sr_2FeTaO_6 (S300-48).

Samples	BET surface area ($m^2 g^{-1}$)	Total Pore Volume ($mL g^{-1}$)
S260-48	37.22	0.10
S300-8	38.72	0.11
S300-16	40.97	0.13
S300-32	39.65	0.12
S300-48	38.54	0.11

gap of Sr_2FeTaO_6 , and the I_{max} value reaches to 0.38 mV, bigger than that of S300-48 (0.27 mV), which suggests that a large amount of excess electrons is injected from Sr_2FeTaO_6 into the CB of $NaTaO_3$ because only Sr_2FeTaO_6 can be excited under visible light in sample S300-16 heterojunction. However, the I_{max} value of sample S-MIXT (0.29 mV) is much smaller than that of S300-16 heterojunction, indicating that, compared with the heterojunction fabrication strategy, photo-induced electrons transferring from Sr_2FeTaO_6 to $NaTaO_3$ is more difficult for sample S-MIXT by a mechanical mixing method, and in other words, the special interfacial structure of S300-16 heterojunction is more conducive for the electron transferring.

Finally, the band edge positions were quantitatively evaluated by measuring the Mott-Schottky plots of the prepared photoelectrodes at a pH value of 7.0 which closed to the pH environment for photocatalytic hydrogen evolution reaction tests. Fig. 13 displays the Mott-Schottky

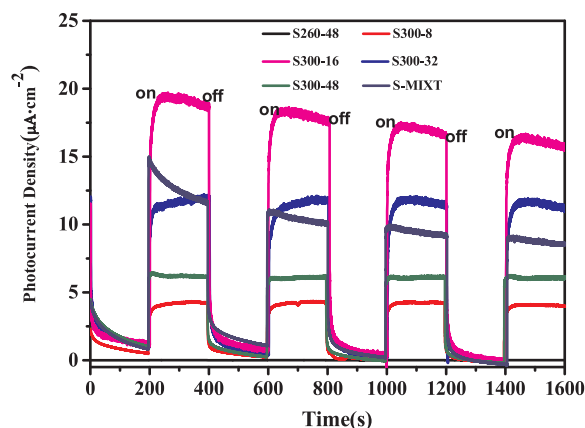


Fig. 10. Photocurrent plots of pure $NaTaO_3$ (S260-48), $Sr_2FeTaO_6/NaTaO_3$ heterojunctions (S300-8, S300-16, S300-32), pure Sr_2FeTaO_6 (S300-48), and mechanical mixture (S-MIXT).

plots for as-prepared photoelectrodes. Both samples show a positive slop in the linear region, indicative of n-type semiconductor [19]. The flat band potential, determined from the extrapolation of the linear curve to the axis, arranges in the order of -0.59 and -0.22 V (vs RHE) for sample S260-48 and S300-48, respectively. It is generally known that the bottom of the conduction bands of n-type semiconductors is

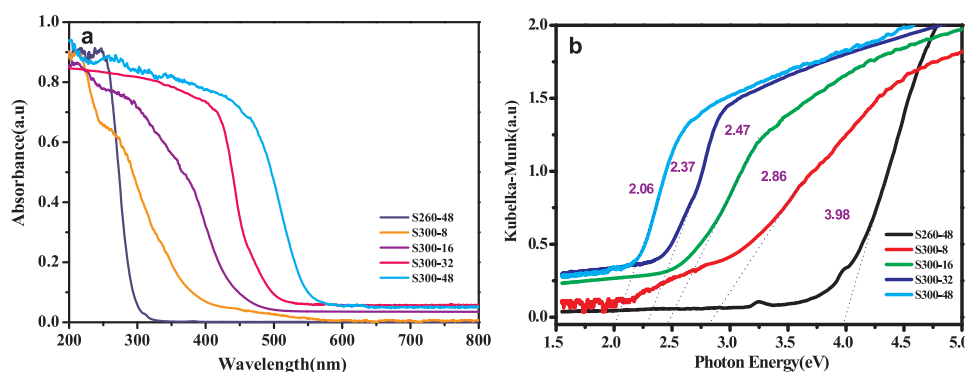


Fig. 9. (a) UV-vis diffuse reflectance spectra, and (b) plots of Kubelka-Munk versus photon energy ($h\nu$) of pure $NaTaO_3$ (S260-48), $Sr_2FeTaO_6/NaTaO_3$ heterojunctions (S300-8, S300-16, S300-32), and pure Sr_2FeTaO_6 (S300-48).

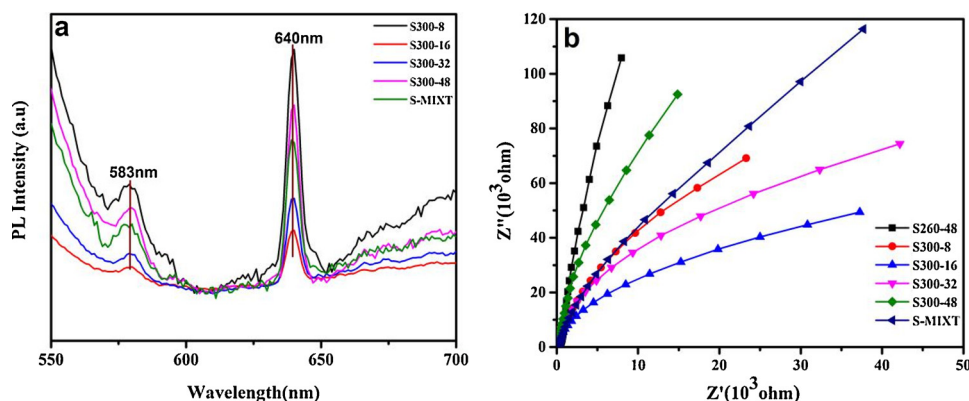


Fig. 11. (a) Room-temperature PL spectra of pure $\text{Sr}_2\text{FeTaO}_6$ (S300-48), $\text{Sr}_2\text{FeTaO}_6/\text{NaTaO}_3$ heterojunctions (S300-8, S300-16, S300-32), and S-MIXT, (excitation at 470 nm); (b) EIS Nyquist plots of pure NaTaO_3 (S260-48), $\text{Sr}_2\text{FeTaO}_6/\text{NaTaO}_3$ heterojunctions (S300-8, S300-16, S300-32), pure $\text{Sr}_2\text{FeTaO}_6$ (S300-48), and mechanical mixture (S-MIXT).

more negative by ca. 0.2 V than the flat band potential [41], so the conduction band (CB) minimum of the n-type sample S260-48 and S300-48 is estimated to be -0.79 and -0.42 eV (vs RHE), respectively. Combined with the band gap values obtained from UV-Vis spectra characterization, the valence band (VB) maximum of these samples should be located at 3.19 and 1.64 eV, respectively.

As mentioned above, introducing narrow-bandgap $\text{Sr}_2\text{FeTaO}_6$ into wide-bandgap NaTaO_3 for in situ fabricating the $\text{Sr}_2\text{FeTaO}_6/\text{NaTaO}_3$ heterojunctions has played an important role in the effective promotion of electron-hole separation and visible-light absorption. The different photocatalytic activities of as-synthesized S300-8, S300-16, and S300-32 heterojunctions mainly originated from the different photo-induced electron transferring efficiency and visible-light absorption, which was related to the heterojunction structure of contact interface and molar ratio of phase composition. Compared with the interfacial structure and photocatalytic activities of sample S300-8, S300-16, and S300-32, the space of heterojunction transitional zone S is 0.25, 0.35, and 0.45 nm, and the molar ratio of $\text{Sr}_2\text{FeTaO}_6$ to NaTaO_3 is 0.18, 0.53, and 1.17, respectively. Correspondingly, the photocatalytic hydrogen evolution rate is 664, 1334, and $904 \mu\text{mol h}^{-1} \cdot \text{g}^{-1}$, and the NO removal ratio η (%) is 40, 72, and 59%, respectively. Why does the heterojunction with S at 0.35 nm have the optimal photo-induced electron transferring and separating efficiency? The important and interesting question would be answered from bonding process in atomic level. For the monoclinic phase NaTaO_3 (JCPDS No.74-2481), the Ta-O bond length is 0.19915 nm, Ta-O-Ta bond angle is 180° , and O-Ta-O bond angle is 180° or 90° . During the fabrication of heterojunction structure, the monoclinic phase NaTaO_3 interface exposes the majority of O atomic terminal, and minority of Ta atomic terminal because of oxygen vacancy. For the orthorhombic phase $\text{Sr}_2\text{FeTaO}_6$ (JCPDS No.88-0135), the Fe/Ta-O bond length is 0.19984–0.19994 nm, Fe/Ta-O-Fe/Ta bond angle is 165.13 and 172.26° , and O-Fe/Ta-O bond angle is 90.3 , 90.77 , and

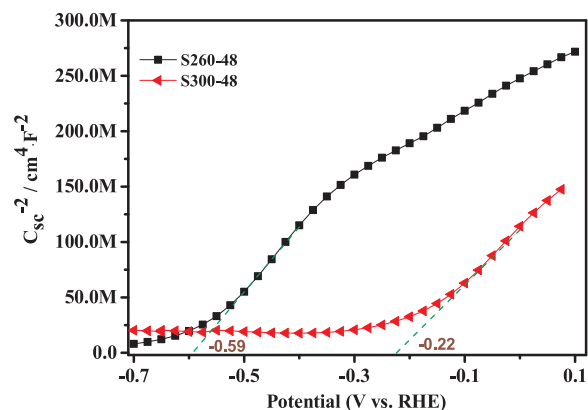


Fig. 13. Mott-Schottky plot of pure NaTaO_3 (S260-48) and pure $\text{Sr}_2\text{FeTaO}_6$ (S300-48) electrodes. Electrolyte: 15 vol% TEOA solution (pH = 7.0). Frequency: 1000 HZ.

92.97° . The orthorhombic phase $\text{Sr}_2\text{FeTaO}_6$ interface exposes the majority of Ta/Fe atomic terminal, and minority of O atomic terminal. Undoubtedly, a well-defined $\text{Sr}_2\text{FeTaO}_6/\text{NaTaO}_3$ heterojunction is fabricated by bonding method between the O, Ta atomic terminal of NaTaO_3 and Fe, Ta, O atomic terminal of $\text{Sr}_2\text{FeTaO}_6$ in the transitional zone, which acted as a 'highway' tunnel for the rapid transferring of photo-generated charge carriers. And so, the space of heterojunction transitional zone S is a crucial factor in bonding process which needs an appropriate bonding distance. As presented in Scheme 2a, b, and c, the $\text{Sr}_2\text{FeTaO}_6/\text{NaTaO}_3$ heterojunction, with $S = 0.25$ nm, is fabricated by the Ta–O–Ta(Fe) bond with the bond angle of 77.5° and the stretched Ta–O weak bond; with $S = 0.35$ nm, fabricated by the Ta–O–Ta(Fe) bond with a bond angle of 122.2° ; and with $S = 0.45$ nm, fabricated by

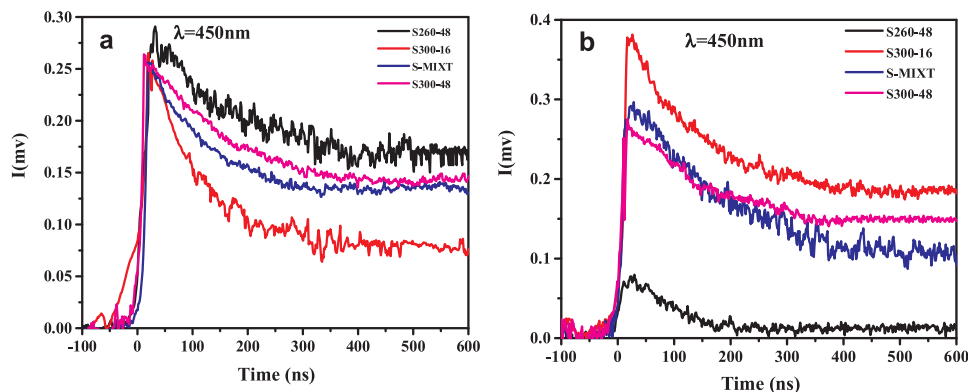
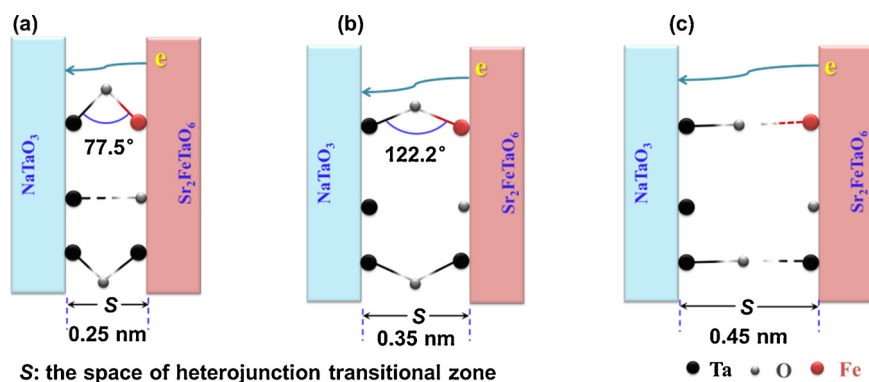


Fig. 12. TRMC signals obtained after excitation at 266 nm (a) and 450 nm (b) of pure NaTaO_3 (S260-48), optimal $\text{Sr}_2\text{FeTaO}_6/\text{NaTaO}_3$ heterojunction (S300-16), pure $\text{Sr}_2\text{FeTaO}_6$ (S300-48), and mechanical mixture (S-MIXT).



Scheme 2. Proposed mechanism of electron transfer through the $\text{Sr}_2\text{FeTaO}_6/\text{NaTaO}_3$ heterojunction.

the stretched Ta–O–Ta(Fe) weak bond. The bond angle of standard Ta–O–Ta(Fe) bond is more closed to 180° and more conducive to the photo-induced electron transferring [20], and thus, the heterojunction with S at 0.35 nm has an appropriate bonding degree which resulted in the optimal photo-induced electron transferring and separating efficiency. Admittedly, the cognition and comprehension about the relations between the space of heterojunction transitional zone and the transferring efficiency of photo-generated charge carriers need more experimental and theoretical evidences in the future works. What we believe is that, the space of heterojunction transitional zone may not be the only factor which influences transferring efficiency of photo-generated charge carriers, but it is certainly an important one.

3.5. Proposed photocatalytic mechanism

To confirm which kinds of active species contributes to the observed photocatalytic removal of NO, a series of trapping experiments were carried out using various scavengers. Explicitly, isopropyl alcohol (IPA), potassium iodide (KI), AgNO_3 , and p-benzoquinone (PBQ) were used as trapping agents for $\cdot\text{OH}$, h^+ , e^- , and $\cdot\text{O}_2^-$, respectively. Fig. 14a shows that in the presence of AgNO_3 , the NO removal efficiency was greatly attenuated. Hence, the photo-induced electron e^- is a main active species. When IPA is added in the system as an $\cdot\text{OH}$ trapper, the same reaction trends were obtained, implying $\cdot\text{OH}$ also is a main active species. However, with the presence of KI, the reaction has no significant change, thus the photo-generated hole h^+ has a little effect on the NO removal reaction. To further confirm the role of superoxide radicals, PBQ is added in the reaction system as an $\cdot\text{O}_2^-$ scavenger. Indeed, the NO removal efficiency is drastically suppressed with addition of PBQ, indicating that $\cdot\text{O}_2^-$ is a contributing intermediate in the NO removal reaction. On the basis of the above experimental findings, it is reasonable to deduce that the removal of NO is through its reaction with $\cdot\text{O}_2^-$ radicals, which is formed by the reaction of surface adsorbed O_2 with photo-induced electrons.

To further identify the radical generation in S300-16 photocatalytic system under visible light irradiation, the ESR spin-trap with DMPO technique was carried out. Fig. 14b presents ESR spectra of sample S300-16 measured under visible light irradiation and dark at room temperature in air. Under the dark condition, no ESR signal was detected. When the light is on, the characteristic signals of the $\text{DMPO}\cdot\cdot\text{O}_2^-$ could be observed, which confirmed that $\cdot\text{O}_2^-$ species was formed during the photocatalytic process. In addition, the characteristic quadruple peaks of the $\text{DMPO}\cdot\cdot\text{OH}$ were also detected, but its peak intensity was extremely low, compared with that of $\text{DMPO}\cdot\cdot\text{O}_2^-$ adducts. Therefore, it can be concluded that the $\cdot\text{O}_2^-$ radicals plays an important role in the photo-degradation process [32].

On the basis of the above discussion, the NO removal process over sample S300-16 can be classified in to step reaction: (i) When the as-obtained samples are irradiated by visible light, the surface adsorbed

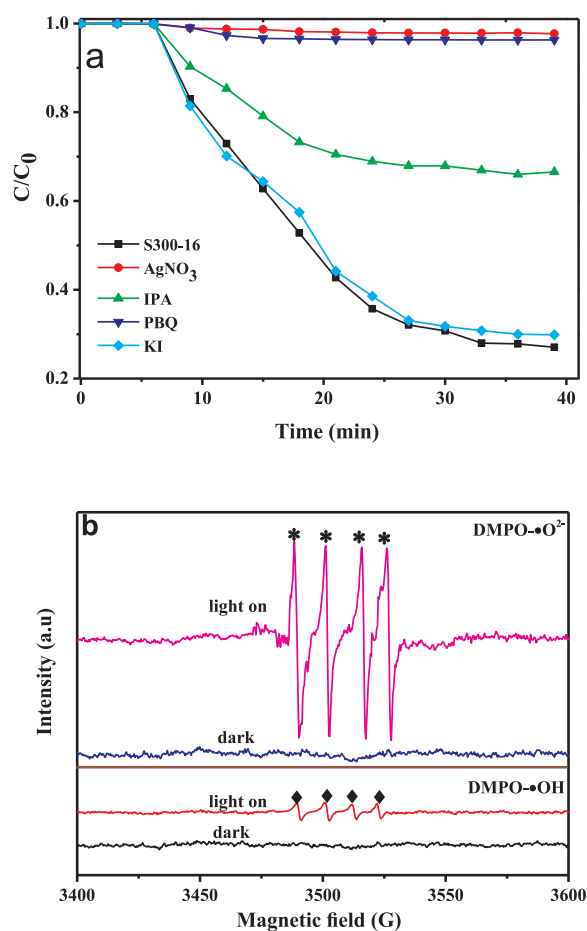
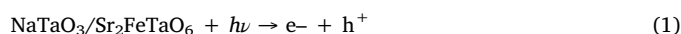
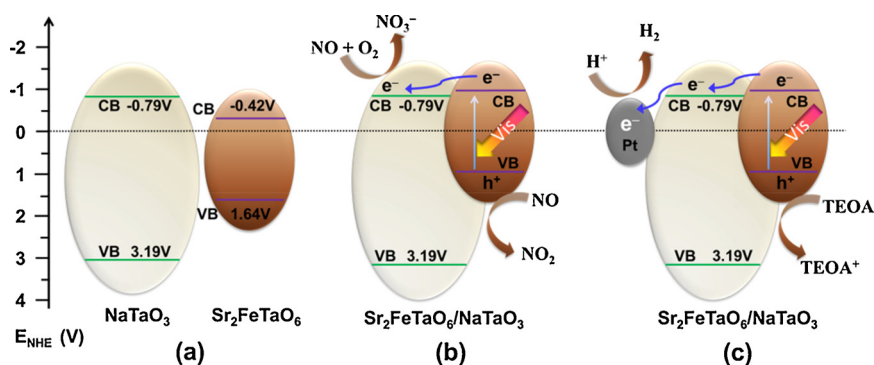


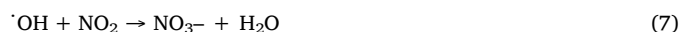
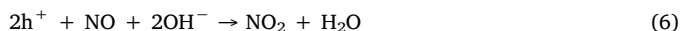
Fig. 14. (a) Photocatalytic trapping experiments of sample S300-16 over NO oxidation under visible light irradiation; (b) DMPO spin-trapping ESR spectra of S300-16 in methanol dispersion for $\text{DMPO}\cdot\cdot\text{O}_2^-$ and in aqueous dispersion for $\text{DMPO}\cdot\cdot\text{OH}$.

oxygen is activated by photo-induced electrons forming super oxide radicals ($\cdot\text{O}_2^-$), which can direct oxidization of NO into nitrite and or nitrate, (ii) the $\cdot\text{O}_2^-$ species was transferred into hydroxyl radical, which further oxide to NO_2 into NO_3^- . However, it can be seen from the photocatalytic activity tests that the formation of NO_2 is not predominant, thus, the direct oxidation of NO to NO_3^- is the main step of NO removal [42]. The possible reaction mechanism of NO oxidation can be summarized as follows:





Scheme 3. Proposed photocatalytic mechanism over the $\text{Sr}_2\text{FeTaO}_6/\text{NaTaO}_3$ heterojunction.



Under visible light illumination, the photocatalytic activity of pure NaTaO_3 is ignorable because the photon energy is much lower than its bandgap energy. All the $\text{Sr}_2\text{FeTaO}_6/\text{NaTaO}_3$ heterojunctions exhibited visible-light-driven photocatalytic NO removal and hydrogen evolution performance, of which sample $\text{Sr}_2\text{FeTaO}_6/\text{NaTaO}_3$ (S300-16) heterojunction exhibits the highest photocatalytic activity under visible light, much higher than that of pure NaTaO_3 and $\text{Sr}_2\text{FeTaO}_6$. The enhanced photocatalytic activity was originated from the electrons transferring from $\text{Sr}_2\text{FeTaO}_6$ to NaTaO_3 , as evidenced by TRMC result, as presented by some recently reported papers [40–45].

Based on the analysis and discussion mentioned above, we propose a conceivable photocatalytic mechanism, as illustrated in Scheme 3a, b, and c. Before connection of NaTaO_3 with $\text{Sr}_2\text{FeTaO}_6$, the CB of NaTaO_3 is lightly negative than that of $\text{Sr}_2\text{FeTaO}_6$ (Scheme 3a), but after connection into heterojunction, under visible light irradiation, the excess electron accumulation in CB of $\text{Sr}_2\text{FeTaO}_6$ leads to band bending and shifting of CB and VB potential towards a more negative region (Scheme 3b and c). As a result, the photo-generated electron-hole pairs were separated and transferred efficiently, increasing the lifetime of the charge carriers for the photocatalytic reactions. As mentioned above, it is reasonable to believe that the excellent photocatalytic performances of $\text{Sr}_2\text{FeTaO}_6/\text{NaTaO}_3$ heterojunction were due to the incorporation of $\text{Sr}_2\text{FeTaO}_6$ for its visible-light response and the intimate interfacial contact between NaTaO_3 and $\text{Sr}_2\text{FeTaO}_6$ for the rapid electron transferring.

4. Conclusions

In this work, $\text{Sr}_2\text{FeTaO}_6/\text{NaTaO}_3$ heterojunctions with intimate interfacial contact were synthesized by a simple temperature-programming hydrothermal process. NaTaO_3 nanosheets were firstly synthesized at a hydrothermal temperature of 260 °C and then rising the temperature to 300 °C, NaTaO_3 nanosheets were partial transformed into $\text{Sr}_2\text{FeTaO}_6$, forming $\text{Sr}_2\text{FeTaO}_6/\text{NaTaO}_3$ heterojunction with intimate interfacial contact. The molar ratio and transitional zone space can be controlled by varying the hydrothermal time. Details of structure and chemical properties were carefully characterized. The as-obtained $\text{Sr}_2\text{FeTaO}_6/\text{NaTaO}_3$ heterojunctions all exhibited photocatalytic performance for NO removal and hydrogen evolution under visible-light irradiation, of which $\text{Sr}_2\text{FeTaO}_6/\text{NaTaO}_3$ heterojunction with a molar

ratio of 0.53 shows the highest photocatalytic activity. The excellent photocatalytic activity was originated from the formation of the intimate interfacial heterojunction and transitional zone space of 0.35 nm between $\text{Sr}_2\text{FeTaO}_6$ and NaTaO_3 , which acted as a ‘highway’ for the rapid transferring of photo-generated charge carriers. The controllable space of heterojunction transitional zone has played an important role in transferring efficiency of photo-generated charge carriers, which presents a new cognitive perspective for constructing efficient heterojunction photocatalyst.

Even the visible-light-driven photocatalytic activity of $\text{Sr}_2\text{FeTaO}_6$ was improved by combined NaTaO_3 , but it was still low for application. Therefore, how to improve the photocatalytic activities of $\text{Sr}_2\text{FeTaO}_6$ -based systems is very important and hard in the future work.

Notes

The authors declare no competing financial interest.

Acknowledgements

This work is supported by the National Natural Science Foundation of China (NSFC) (No. 21703196, 21603182) and the Jiangsu Six Talent Peaks Program (No. XCL-087)

References

- [1] I. Ivanova, T.A. Kandiel, Y.-J. Cho, W. Choi, D. Bahnemann, Mechanisms of photocatalytic molecular hydrogen and molecular oxygen evolution over La-doped NaTaO_3 particles: effect of different cocatalysts and their specific activity, *ACS Catal.* 8 (2018) 2313–2325.
- [2] L. An, T. Sasaki, P.G. Weidler, C. Wöll, N. Ichikuni, H. Onishi, Local environment of strontium cations activating NaTaO_3 photocatalysts, *ACS Catal.* 8 (2018) 880–885.
- [3] E. Cui, Q. Meng, C. Ge, G. Yu, G. Hou, N. Xu, F. Zhang, Y. Wu, The roles of surface oxygen vacancy over $\text{Mg}_4\text{Ta}_2\text{O}_9$ photocatalyst in enhancing visible-light photocatalytic hydrogen evolution performance, *Catalan J. Commun. Cult. Stud.* 103 (2018) 29–33.
- [4] K. Wang, G. Zhang, J. Li, Y. Li, X. Wu, 0D/2D Z-scheme heterojunctions of bismuth tantalate quantum dots/ultrathin g- C_3N_4 nanosheets for highly efficient visible light photocatalytic degradation of antibiotics, *ACS Appl. Mater. Interfaces* 9 (2017) 43704–43715.
- [5] A. Krukowska, M.J. Winiarski, J. Strychalska-Nowak, T. Klimczuk, A. Zaleska-Medynska, Rare earth ions doped $\text{K}_2\text{Ta}_2\text{O}_6$ photocatalysts with enhanced UV–vis light activity, *Appl. Catal. B: Environ.* 224 (2018) 451–468.
- [6] A. Bloesser, P. Voepel, M.O. Loeh, A. Beyer, K. Volz, R. Marschall, Tailoring the diameter of electrospun layered perovskite nanofibers for photocatalytic water splitting, *J. Mater. Chem. A Mater. Energy Sustain.* 6 (2018) 1971–1978.
- [7] F. Fairbrother, *The Chemistry of Niobium and Tantalum*, Elsevier, Amsterdam, 1967.
- [8] T. Grewe, H. Tüysüz, Amorphous and crystalline sodium tantalate composites for photocatalytic water splitting, *ACS Appl. Mater. Interfaces* (2015) 23153–23162.
- [9] H.Y. Yang, S.F. Yu, S.P. Lau, X. Zhang, D.D. Sun, G. Jun, Evidence of a strong electron–hole separation effect in ZnO/TiO_2 core/shell nanowires, *J. Alloys Compd.* 749 (2018) 217–220.
- [10] B. Modak, P. Modak, S.K. Ghosh, Efficient strategy for enhancement of visible light photocatalytic activity of NaTaO_3 by a significant extent, *J. Phys. Chem. C* 121 (2017) 12980–12990.
- [11] X. Chen, B. Zhang, S. Peng, H. Song, B. Liu, S. Guo, B. Gao, J. Fu, X. Zhang, Enhanced photocatalytic activity of perovskite-type NaTaO_3 by effective nitrogen

- doping, *Nanosci. Nanotechnol. Lett.* 9 (2017) 1463–1469.
- [12] M. Li, P. Li, K. Chang, T. Wang, L. Liu, Q. Kang, S. Ouyang, J. Ye, Highly efficient and stable photocatalytic reduction of CO₂ to CH₄ over Ru loaded NaTaO₃, *Chem. Commun. (Camb.)* 51 (2015) 7645–7648.
 - [13] Q. Zhang, Z. Li, S. Wang, R. Li, X. Zhang, Z. Liang, H. Han, S. Liao, C. Li, Effect of redox cocatalysts location on photocatalytic overall water splitting over cubic NaTaO₃ semiconductor crystals exposed with equivalent facets, *ACS Catal.* 6 (2016) 2182–2191.
 - [14] L. Xu, J. Guan, W. Shi, Enhanced interfacial charge transfer and visible photocatalytic activity for hydrogen evolution from a Ta₂O₅-based mesoporous composite by the incorporation of quantum-sized CdS, *ChemCatChem* 4 (2012) 1353–1359.
 - [15] L. Xu, J. Guan, W. Shi, L. Liu, Heterostructured mesoporous In₂O₃/Ta₂O₅ composite photocatalysts for hydrogen evolution: impacts of In₂O₃ content and calcination temperature, *J. Colloid Interface Sci.* 377 (2012) 160–168.
 - [16] K.H. Reddy, S. Martha, K.M. Parida, Facile fabrication of Bi₂O₃/Bi-NaTaO₃ photocatalysts for hydrogen generation under visible light irradiation, *RSC Adv.* 2 (2012) 9423–9436.
 - [17] H. Kato, A. Kudo, New tantalate photocatalysts for water decomposition into H₂ and O₂, *Chem. Phys. Lett.* 295 (1998) 487–492.
 - [18] L. Xu, X. Sun, H. Tu, Q. Jia, H. Gong, J. Guan, Synchronous etching-epitaxial growth fabrication of facet-coupling NaTaO₃/Ta₂O₅ heterostructured nanofibers for enhanced photocatalytic hydrogen production, *Appl. Catal. B: Environ.* 184 (2016) 309–319.
 - [19] H. Chen, X. Xu, Ruddlesden-popper compounds in the double-perovskite family Sr₂FeTaO₆ (SrO)_n (n = 0, 1 and 2) and their photocatalytic properties, *Appl. Catal. B: Environ.* 206 (2017) 35–43.
 - [20] S. Yang, D. Xu, B. Chen, B. Luo, X. Yan, L. Xiao, W. Shi, Synthesis and visible-light-driven photocatalytic activity of p–n heterojunction Ag₂O/NaTaO₃ nanocubes, *Appl. Surf. Sci.* 383 (2016) 214–221.
 - [21] M. Kunst, G. Beck, The study of charge carrier kinetics in semiconductors by microwave conductivity measurements, *J. Appl. Phys.* 60 (1986) 3558–3566.
 - [22] J.M. Warman, M.P. Dehaas, Puls Radiolysis, Chap. 6, CRC Press, 1991 p. 101.
 - [23] Q. Zhao, X. Liu, Y. Xing, Z. Liu, C. Du, Synthesizing Bi₂O₃/BiOCl heterojunctions by partial conversion of BiOCl, *J. Mater. Sci.* 52 (2017) 2117–2130.
 - [24] L. An, Y. Park, Y. Sohn, H. Onishi, Effect of etching on electron-hole recombination in Sr-Doped NaTaO₃ photocatalysts, *J. Phys. Chem. C* 119 (2015) 28440–28447.
 - [25] S.F. Ho, S. Contarini, J.W. Rabalais, Ion-beam-induced chemical changes in the oxyanions (MO₃ⁿ⁻) and oxides (MO_x) Where M = Cr, Mo, W, V, Nb, and Ta, *J. Phys. Chem.* 91 (1987) 4779–4788.
 - [26] V.V. Atuchin, J.-C. Grivel, Z. Zhang, Core level photoemission spectroscopy and chemical bonding in Sr₂Ta₂O₇, *Chem. Phys.* 360 (2009) 74–78.
 - [27] E.-L. Rautama, T.S. Chan, R.S. Liu, J.M. Chen, H. Yamauchi, M. Karpinen, Electron-doping through LaIII-for-SrII substitution in (Sr_{1-x}La_x)₂FeTaO₆: effects on the valences and ordering of the B-site cations, Fe and Ta, *J. Solid State Chem.* 179 (2006) 111–116.
 - [28] J. Di, Xia J, M. Ji, B. Wang, S. Yin, Q. Zhang, Z. Chen, H. Li, Carbon quantum dots modified BiOCl ultrathin nanosheets with enhanced molecular oxygen activation ability for broad spectrum photocatalytic properties and mechanism insight, *ACS Appl. Mater. Interfaces* 7 (2015) 20111–20123.
 - [29] T. Danno, D. Nakatsuka, Y. Kusano, H. Asaoka, M. Nakanishi, T. Fujii, Y. Ikeda, J. Takada, Crystal structure of β-Fe₂O₃ and topotactic phase transformation to α-Fe₂O₃, *Cryst. Growth Des.* 13 (2013) 770–774.
 - [30] W. Cui, W. An, L. Liu, J. Hu, Y. Liang, Novel Cu₂O quantum dots coupled flower-like BiOBr for enhanced photocatalytic degradation of organic contaminant, *J. Hazard. Mater.* 280 (2014) 417–427.
 - [31] X.F. Zhang, L.L. Du, H. Wang, X.L. Dong, X.X. Zhang, C. Ma, H.C. Ma, Highly ordered mesoporous BiVO₄: controllable ordering degree and super photocatalytic ability under visible light, *Microporous Mesoporous Mater.* 173 (2013) 175–180.
 - [32] Z.Y. Zhang, D.L. Jiang, D. Li, M.Q. He, M. Chen, Construction of SnNb₂O₆ nanosheet/g-C₃N₄ nanosheet two-dimensional heterostructures with improved photocatalytic activity: synergistic effect and mechanism insight, *Appl. Catal. B-Environ* 183 (2016) 113–123.
 - [33] H. Fu, S. Zhang, L. Zhang, Y. Zhu, Visible-light-driven NaTaO_{3-x}N_x catalyst prepared by a hydrothermal process, *Mater. Res. Bull.* 43 (2008) 864–872.
 - [34] G. He, C. Xing, X. Xiao, R. Hu, X. Zuo, J. Nan, Facile synthesis of flower-like Bi₁₂O₁₇Cl₂/β-Bi₂O₃ composites with enhanced visible light photocatalytic performance for the degradation of 4-tert-butylphenol, *Appl. Catal. B: Environ.* 170–171 (2015) 1–9.
 - [35] G.H. Zhang, W.S. Guan, H. Shen, X. Zhang, W.Q. Fan, C.Y. Lu, H.Y. Bai, L.S. Xiao, W. Gu, W.D. Shi, Organic additives-free hydrothermal synthesis and visible-light-driven photodegradation of tetracycline of WO₃ nanosheets, *Ind. Eng. Chem. Res.* 53 (2014) 5443–5450.
 - [36] X.L. Xu, Y.Y. Zhao, E.J. Sie, Y.H. Lu, S.A. Ekahana, X. Ju, Q. Jiang, J.B. Wang, H.D. Sun, T.C. Sum, C.H. Huan, Y.P. Feng, Q. Xiong, Dynamics of bound exciton complexes in CdS nanobelts, *ACS Nano* 5 (2011) 3660–3669.
 - [37] W.H. Leng, Z. Zhang, J.Q. Zhang, C.N. Cao, Investigation of the kinetics of a TiO₂ photoelectro-catalytic reaction involving charge transfer and recombination through surface states by electrochemical impedance spectroscopy, *J. Phys. Chem. B* 109 (2005) 15008–15023.
 - [38] Y. Wang, R. Shi, J. Lin, Y. Zhu, Significant photocatalytic enhancement in methylene blue degradation of TiO₂ photocatalysts via graphene-like carbon in situ hybridization, *Appl. Catal. B: Environ.* 100 (2010) 179–183.
 - [39] C. Colbeau-Justin, M. Kunst, Structural influence on charge-carrier lifetimes in TiO₂ powders studied by microwave absorption, *J. Mater. Sci.* 38 (2003) 2429–2437.
 - [40] M.G. Mendez-Medrano, E. Kowalska, A. Lehoux, A. Herissan B. Ohtani, D. Bahena, V. Briois, C. Colbeau-Justin, J.L. Rodríguez-Lopez, H. Remita, Surface modification of TiO₂ with Ag nanoparticles and CuO nanoclusters for application in photocatalysis, *J. Phys. Chem. C* 120 (2016) 5143–5154.
 - [41] S. Chen, Y. Qi, G. Liu, J. Yang, F. Zhang, C. Li, A wide visible-light-responsive tunneled MgTa₂O_{6-x}N_x photocatalyst for water oxidation and reduction, *Chem. Commun. (Camb.)* 50 (2014) 14415–14417.
 - [42] J. Hu, D. Chen, N. Li, Q. Xu, H. Li, J. He, J. Lu, In situ fabrication of Bi₂O₃CO₃/MoS₂ on carbon nanofibers for efficient photocatalytic removal of NO under visible-light irradiation, *Appl. Catal. B: Environ.* 217 (2017) 224–231.
 - [43] B. Li, Y. Hao, B. Zhang, X. Shao, L. Hu, A multifunctional noble-metal-free catalyst of CuO/TiO₂ hybrid Nanofibers, *Appl. Catal. A Gen.* 531 (2017) 1–12.
 - [44] I. Mondal, U. Pal, Synthesis of MOF templated Cu/CuO@TiO₂ nanocomposites for synergistic hydrogen production, *Phys. Chem. Chem. Phys.* 18 (2016) 4780–4788.
 - [45] M. Lei, N. Wang, L.H. Zhu, Q.L. Zhou, G. Nie, H.Q. Tang, Photocatalytic reductive degradation of polybrominated diphenyl ethers on CuO/TiO₂ nanocomposites: a mechanism based on the switching of photocatalytic reduction potential being controlled by the valence state of copper, *Appl. Catal. B: Environ.* 182 (2016) 414–423.